The Astrophysical Journal, 730:137 (15pp), 2011 April 1 doi:10.1088/0004-637X/730/2/137

THE MASS–METALLICITY AND LUMINOSITY–METALLICITY RELATIONS FROM DEEP2 AT $z \sim 0.8$

H. J. Zahid, L. J. Kewley, and F. Bresolin
Institute for Astronomy, 2680 Woodlawn Dr., Honolulu, HI 96822, USA
Received 2010 April 28; accepted 2011 January 28; published 2011 March 15

ABSTRACT

We present the mass–metallicity (MZ) and luminosity–metallicity (LZ) relations at $z \sim 0.8$ from ∼1350 galaxies in the Deep Extragalactic Evolutionary Probe 2 survey. We determine stellar masses by fitting the spectral energy distribution inferred from photometry with current stellar population synthesis models. This work raises the number of galaxies with metallicities at $z \sim 0.8$ by more than an order of magnitude. We investigate the evolution in the MZ and LZ relations in comparison with local MZ and LZ relations determined in a consistent manner using ∼21,000 galaxies in the Sloan Digital Sky Survey. We show that high stellar mass galaxies ($M \sim 10^{10.6}\,M_{\odot}$) at $z \sim 0.8$ have attained the chemical enrichment seen in the local universe, while lower stellar mass galaxies ($M \sim 10^{9.2}\,M_{\odot}$) at $z \sim 0.8$ have lower metallicities ($\Delta\log(\mathrm{O/H}) \sim 0.15$ dex) than galaxies at the same stellar mass in the local universe. We find that the LZ relation evolves in both metallicity and *B*-band luminosity between $z \sim 0.8$ and $z \sim 0$, with the *B*-band luminosity evolving as a function of stellar mass. We emphasize that the *B*-band luminosity should not be used as a proxy for stellar mass in chemical evolution studies of star-forming galaxies. Our study shows that both the metallicity evolution and the *B*-band luminosity evolution for emission-line galaxies between the epochs are a function of stellar mass, consistent with the cosmic downsizing scenario of galaxy evolution.

Key words: galaxies: abundances – galaxies: evolution – galaxies: high-redshift

Online-only material: color figures

1. INTRODUCTION

The heavy-element abundance in galaxies is a key physical property for understanding galaxy evolution. Metals are formed in massive stars and are dispersed into the interstellar medium (ISM) via mass-loss processes. Hence, metallicity provides an important record of the star formation history of a galaxy. Galaxies and their chemical abundances, however, do not evolve as closed systems where metals are dispersed into the ISM as gas is converted into stars. Rather, they are modulated by inflow of unenriched gas (e.g., Kewley et al. 2010) and a complex "feedback" mechanism where supernovae and stellar winds influence the ISM by inducing outflows of gas into the intergalactic medium (IGM) and regulating star formation through reheating (Larson 1974; Larson & Dinerstein 1975; Kauffmann & Charlot 1998; Somerville & Primack 1999; Springel & Hernquist 2003).

A simple "closed-box" model in which feedback is not considered predicts a correlation between two fundamental parameters—mass and metallicity (van den Bergh 1962; Schmidt 1963; Searle & Sargent 1972; Erb et al. 2006). The pioneering work of Lequeux et al. (1979) first showed this correlation in local irregular galaxies. Many subsequent efforts have focused on the relation between luminosity and metallicity (Skillman et al. 1989; Zaritsky et al. 1994; Garnett et al. 1997; Lamareille et al. 2004; Salzer et al. 2005) where luminosity is taken as a proxy for mass because of the difficulty in inferring galaxy masses from observables. Early attempts to extend this relation to intermediate redshifts found that the luminosity–metallicity (LZ) relation at earlier epochs was consistent with the local universe (Kobulnicky et al. 1999; Carollo & Lilly 2001). However, many recent investigations have provided compelling evidence for evolution of the LZ relation over cosmological times (Kobulnicky & Koo 2000; Pettini et al. 2001; Kobulnicky et al. 2003; Kobulnicky & Kewley 2004; Maier et al. 2004; Shapley et al. 2004, 2005). Luminosities of galaxies evolve along with their chemical abundances on cosmological timescales and disentangling the contribution for each has posed difficulties in these studies.

Evolution in the LZ relation implies an evolution in the more fundamental mass–metallicity (MZ) relation. Development of more sophisticated models for stellar population synthesis (Bruzual & Charlot 2003) and gaseous nebula (Ferland 1996; Charlot & Longhetti 2001) allowed Tremonti et al. (2004, hereafter T04) to establish and quantify the local MZ relation for ∼53,000 star-forming galaxies from the Sloan Digital Sky Survey (SDSS). They found that metallicity increases linearly with stellar mass for galaxies having masses between $10^{8.5}\,M_{\odot}$ and $10^{10.5}\,M_{\odot}$ and flattens out at higher masses. They attribute this depletion of metals in less massive galaxies to ubiquitous galactic winds that strip metals more effectively from galaxies with shallow potential wells, dispersing them into the IGM. Alternatively, it has been suggested that low-mass systems have ongoing star formation and have yet to convert much of their gas into stars and therefore are less evolved, less metal-rich systems as compared to more massive galaxies which have undergone rapid star formation (Brooks et al. 2007; de Rossi et al. 2007; Mouchine et al. 2008). Finally, a varying galaxy-integrated initial mass function (IMF) has also emerged as a possible explanation for the observed MZ relation (Köppen et al. 2007).

Cosmological hydrodynamic simulations (Brooks et al. 2007; Oppenheimer & Davé 2008) have predicted an evolution in the MZ relation and recent observations at intermediate redshifts ($z \sim 0.7$) have provided strong evidence for an evolution. Using the Gemini Deep Deep Survey, Savaglio et al. (2005) first showed the MZ relation beyond the local universe for galaxies at $z = 0.4$–1.0. Their relation intersects the local relation at $M \sim 10^{10.4}\,M_{\odot}$ but is ∼0.3 dex lower at $M \sim 10^{9.3}\,M_{\odot}$, implying a much steeper slope. They conclude that the slope of the MZ relation must become flatter over time. Cowie & Barger (2008) found a difference >0.2 dex for a redshift range of

$0.475 < z < 0.9$ with a similar slope. More recently, Lamareille et al. (2009) find a flatter slope in the MZ relation out to $z \sim 0.9$ and an average difference in metallicity of ∼0.2 dex. To date, the MZ relation has been extended beyond $z \sim 3$ (Shapley et al. 2005; Erb et al. 2006; Maiolino et al. 2008; Pérez-Montero et al. 2009; Mannucci et al. 2009). All these studies have shown evidence of evolution but rigorous quantitative analysis has been hampered by disparate results and small sample sizes leaving the MZ relation at higher redshifts quantitatively uncertain.

In this paper, we present results of our study determining the MZ and LZ relations for galaxies in the redshift range of $0.75 < z < 0.82$. We infer metallicities from gas-phase oxygen abundances using strong-line diagnostics (Pagel et al. 1979; Kewley & Dopita 2002; Kewley & Ellison 2008, hereafter KE08). We make use of publicly available data from the Deep Extragalactic Evolutionary Probe 2 (DEEP2; Davis et al. 2003). We measure the MZ and LZ relations from 1348 galaxies, a substantial increase in the number of objects studied in this redshift range to date. We note that a large sample of galaxies with metallicity and stellar mass determinations in such a small redshift range is ideal for reliably constraining the MZ relation at a specific redshift. In Section 2, we present our criteria for the selection of galaxies and properties of our selected sample. In Section 3, we describe our method for determining masses, our correction for underlying Balmer absorption, and our method for determining masses. In Section 4, we present our derived MZ and LZ relations. In Section 5, we present a discussion of our results. Here we compare the MZ and LZ relations and infer the *B*-band luminosity and evolution as a function of stellar mass and we compare our MZ relation with relations derived by other authors at similar redshifts. We summarize our results in Section 6. Where necessary, we adopt the standard cosmology $(H_0, \Omega_m, \Omega_\Lambda) = (70\,\mathrm{km\,s^{-1}\,Mpc^{-1}}, 0.3, 0.7)$.

2. THE DATA

2.1. DEEP2 Survey Data

Our $z \sim 0.8$ sample comes from the DEEP2 survey. The DEEP2 team used the DEIMOS (Faber et al. 2003) multi-object spectrograph on the Keck telescope to measure spectra for galaxies in four fields covering 3.5 $\mathrm{deg^2}$ down to a limiting magnitude of $R_{\mathrm{AB}} = 24.1$. The survey contains spectra for ∼50,000 galaxies, the majority of which are in the redshift range $0.7 < z < 1.4$. The relatively high-resolution ($R \geqslant 5000$) spectra cover the nominal spectral range 6500–9100 Å. For this study, we used the third data release[1] data and the one-dimensional spectra were obtained from the Horne extraction (Horne 1986).

BRI photometry was obtained by the DEEP2 team for these objects from imaging carried out using the CFH12K camera on the 3.6 m Canada–France–Hawaii Telescope (CFHT; Coil et al. 2004). For a subsample of the data, K_s-band photometry was available in addition to the *BRI* photometry. These data were obtained using the Wide Field Infrared Camera on the 5 m Hale telescope at Mt. Palomar (Bundy et al. 2006). All magnitudes in this study are in the AB system.

2.2. Data Selection

From the 46,337 unique objects in the survey, we begin by selecting 31,656 galaxies for which we have secure redshift determinations from the DEEP2 team ($Q \geqslant 3$, see the Web site for more details). For our determination of metallicity, we use the R_{23} strong-line diagnostic, first calibrated by Pagel et al. (1979). We apply a more recent R_{23} calibration based on the stellar population synthesis and photoionization model calibrations from Kewley & Dopita (2002), and updated in Kobulnicky & Kewley (2004). In the text, we refer to this calibration as KK04. The R_{23} method is a parameterization of metallicity as a function of the ratio of the oxygen nebular emission ([O II] λ3727 doublet, [O III] λ4959, and [O III] λ5007) to Hβ. The method is formally defined in Section 3.3. Given the nominal spectral range of the DEEP2 survey, we can sufficiently bracket the required emission lines within the $0.75 < z < 0.82$ redshift range. Due to a varying object position on the slit mask, the actual spectral range varies from object to object and we require that the spectra cover the wavelength range of 3720–5020 Å, leaving us with 2738 galaxies. We were unable to measure the metallicity in 234 galaxies due to our inability to fit the oxygen or Hβ emission lines, leaving us with 2504 galaxies.

We calculate the R_{23} ratios using the continuum-normalized flux (see the Appendix for full description). In the Appendix, we show that the pseudo-EW is equal, to within the errors, to the EW and refer to it hereafter as the EW. The errors on our EW and line ratio determination come from propagating the measurement uncertainties in the spectrum. In selecting galaxies for analysis, we require that the S/N H$\beta > 3$, EW(Hβ) > 4 Å, and the error in the R_{23} line ratio be less than 2. At high metallicities, the line strength of the [O II] and [O III] line diminishes due to the effectiveness of line cooling of the H II region. In order to avoid biasing our MZ relation to lower metallicities, we do not place a signal-to-noise ratio (S/N) cut on these lines. We normalize the line flux to the continuum by fitting a polynomial to the underlying continuum and dividing the spectrum by this fit. We require that the fit to the continuum be $1\sigma_c$ above zero, where σ_c is the standard deviation of the line-subtracted spectrum (see the Appendix for more detail). These cuts leave us with 1713 galaxies.

Strong-line methods of metallicity determination assume a star-forming population of galaxies and are not applicable to active galactic nuclei (AGNs). We identify all galaxies with $\log(R_{23}) > 1$ as AGNs and remove them from our sample (L. J. Kewley et al. 2011, in preparation). Furthermore, using the color separation for blue and red galaxies parameterized by Willmer et al. (2006) for the DEEP2 survey, Weiner et al. (2007) conclude that a very small fraction of blue galaxies have AGNs whereas at least half of the red galaxies with detectable emission lines show evidence of AGN emission. Similar to T04, we select the blue star-forming galaxies to analyze, as described in the following section. We remove the red galaxies from our sample and are left with 1631 blue emission-line galaxies. The first and second columns of Table 1 summarize our selection. The median for EW(Hβ), S/N Hβ, and σ_{R23} of our selected sample is 12.1, 10.0, and 0.65, respectively.

2.3. Properties of Selected Sample

Willmer et al. (2006) studied the red and blue galaxy luminosity functions by dividing the DEEP2 sample at the trough of the bimodal $U-B$ color distribution. The *U*- and *B*-band absolute magnitudes are synthesized by relating the observed magnitudes to spectral energy distributions (SEDs) of nearby galaxies and inferring a rest-frame absolute magnitude from this SED. We follow a similar procedure and synthesize the *U*- and *B*-band absolute magnitudes using the filters of Buser (1978) and Ažusienis & Straižys (1969), respectively. The red

[1] http://deep.berkeley.edu/DR3/

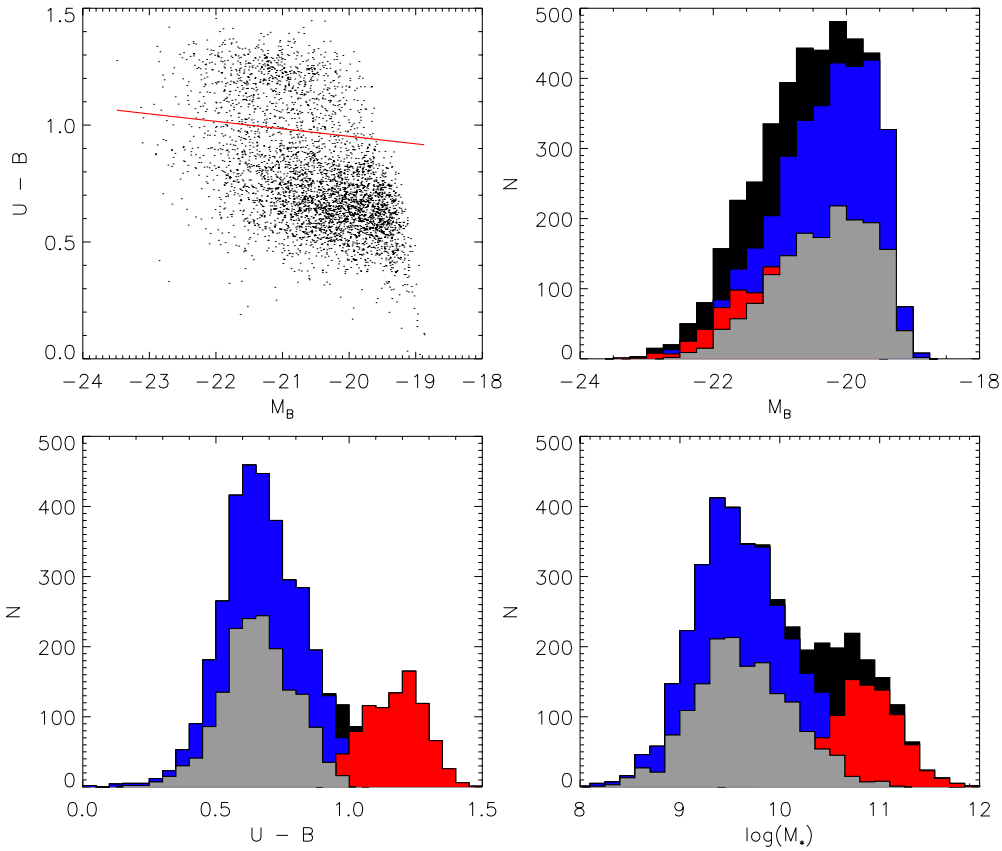

Figure 1. Top left panel shows the color–magnitude diagram of the full sample of 4198 galaxies with the required wavelength coverage from which we make our selection. The red line is the blue–red color division given by Equation (1). The black histogram in each of the other three panels is for the full sample. The blue and red histograms are for the blue and red galaxies within the full sample and the gray histogram is for our selected subsample of 1631 galaxies. The top right panel shows the distribution of the absolute *B*-band magnitude. The bottom left panel shows the color distribution and the bottom right panel shows the mass distribution.

(A color version of this figure is available in the online journal.)

Table 1
Sample Selection

Selection Criteria	Total	Blue	Red
Total number of unique objects	46,337	...	...
Galaxies with secure redshift determination	31,656	...	...
Galaxies with redshifts $0.75 < z < 0.82$	4,198	3,323	875
Rest-frame wavelength cover 3720–5020 Å	2,738	2,152	586
Measured metallicities	2,504	2,117	387
SN H$\beta > 3$	2,168	1,996	172
EW(Hβ) > 4 Å	1,973	1,902	71
$\sigma_{R23} < 2$	1,751	1,702	49
Robust continuum	1,713	1,665	48
Not AGN	1,679	1,631	48
Blue star-forming galaxies	1,631	1,631	0

Notes. The first column gives the particular selection criteria and the second column gives the total number of galaxies that meet this and all criteria above it in the table. The third and fourth columns split the total number of galaxies into blue and red subsamples as defined by Equation (1).

Table 2
Median Properties of the DEEP2 Galaxies

Sample	$U-B$	M_B	Mass $\log(M/M_\odot)$
DEEP2 Full	0.72	−20.4	9.80
DEEP2 Red	1.18	−21.1	10.85
DEEP2 Blue	0.67	−20.2	9.62
DEEP2 Selected	0.66	−20.3	9.59

Notes. The median properties of the data. In the first column, we identify the four samples. The next three columns give the median $U-B$ color, absolute *B*-band magnitude, and mass for each of these samples.

and blue galaxy color division found by Willmer et al. (2006) is given by

$$U - B = 1.0\text{–}0.032(M_B + 21.5). \quad (1)$$

The color division has been converted to AB magnitudes using Table 1 of Willmer et al. (2006). In Columns 3 and 4 of Table 1, we examine the cuts from our selection with respect to the galaxy color.

The top left panel of Figure 1 shows the color–magnitude diagram and the solid red line is the color division given by Equation (1). The other three panels give the absolute *B*-band magnitude, stellar mass (derived in Section 3.1), and $U-B$ color distribution, respectively. The black histogram gives the full sample of 4198 DEEP2 galaxies between $0.75 < z < 0.82$. We refer to this sample as the DEEP2 Full sample. Using the $U-B$ color division, we split the DEEP2 Full sample into subsamples of red and blue galaxies. The histograms of these subsamples are plotted in red and blue and we refer to these subsamples as the DEEP2 Red and DEEP2 Blue samples, respectively. The gray histogram is the distribution of our selected sample of 1631 galaxies described in Section 2.2 and we refer to this as our DEEP2 Selected sample. The median properties of these samples are given in Table 2.

The absolute *B*-band magnitude distribution in the top right panel of Figure 1 shows a range of $-19.0 > M_B > -23$ for the

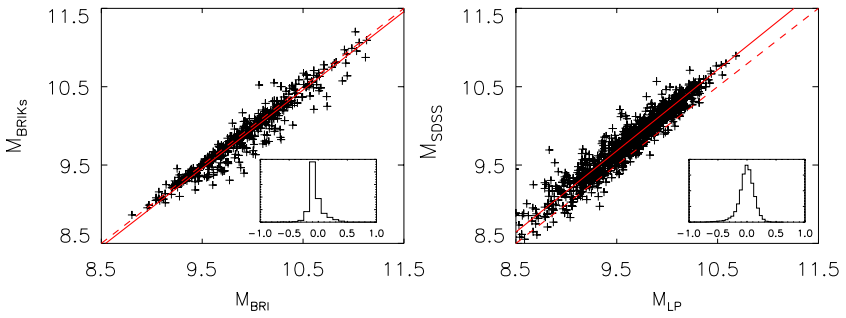

Figure 2. Comparison of stellar mass estimates. The left panel shows the mass estimates using *BRI*-band photometry (M_{BRI}, *x*-axis) as compared with *BRIK*$_s$-band photometry (M_{BRIKs}, *y*-axis). The right panel compares mass estimates made using Le Phare ($M_{\rm LP}$, *x*-axis) and those provided by the MPA/JHU team ($M_{\rm SDSS}$, *y*-axis). The dashed line in each plot is the one-to-one correspondence of the two data sets. The solid line is a bisector fit to the data. The sub-panel in each of the plots shows a histogram of the differences between the two estimates with −0.04 and 0.19 dex added as corrections to the M_{BRI} and $M_{\rm LP}$ mass estimates, respectively.

(A color version of this figure is available in the online journal.)

DEEP2 Full sample. Faber et al. (2007) showed that luminosity functions derived for blue galaxies from the DEEP2 data have an $M_B^* = -21.15$ in our selected redshift range. Our DEEP2 Selected sample consists of galaxies around the knee of the blue galaxy luminosity function (Schechter 1976) with ∼15% (245/1631) of our Galaxies brighter than M_B^*. The bottom left panel of Figure 1 shows that the $U-B$ color range is $0 < U-B < 1.5$ for the DEEP2 Full sample. The color division between red and blue is at $U-B \sim 1$ and the bimodal distribution is clearly highlighted by the well-separated peaks in the blue and red histograms. The bimodal color distribution separates red early-type galaxies from blue late-type star-forming galaxies (Strateva et al. 2001; Hogg et al. 2003; Baldry et al. 2004; Willmer et al. 2006). The mass distribution shown in the bottom right panel of Figure 1 reflects this bimodality, whereby the red galaxies in our sample are not only brighter, but more massive and separated from the lower mass blue galaxies.

By comparing the histograms and median properties in Figure 1, it is clear that the DEEP2 Red sample of galaxies is brighter and more massive than the DEEP2 Blue sample. However, when comparing the histograms and median properties of our DEEP2 Selected sample, which is comprised solely of blue galaxies, with the DEEP2 Blue sample, there is no selection bias toward the brighter or more massive galaxies as one may expect given the selection criteria. We conclude from the comparison of the properties of the DEEP2 Selected and DEEP2 Blue samples that our selected galaxies are representative of the population of blue star forming of galaxies in the DEEP2 survey at $0.75 < z < 0.8$.

3. DATA ANALYSIS

3.1. Stellar Mass Determination

We estimate galaxy stellar masses by comparing photometry with stellar population synthesis models in order to determine the mass-to-light ratio (Bell et al. 2003; Fontana et al. 2004). We use the Le Phare[2] code developed by S. Arnouts and O. Ilbert to estimate the galactic stellar mass. Le Phare is a set of FORTRAN routines developed to determine the photometric redshifts of galaxies. If the redshift is known, it can be held fixed while other physical parameters of the galaxy are determined (i.e., stellar mass) by SED fitting.

The stellar templates of Bruzual & Charlot (2003) and an IMF described by Chabrier (2003) are used to synthesize magnitudes. The 27 models span three metallicities and seven exponentially decreasing star formation models (SFR $\propto e^{-t/\tau}$) with $\tau = 0.1, 0.3, 1, 2, 3, 5, 10, 15$, and 30 Gyr. We apply the extinction law of Calzetti et al. (2000) allowing $E(B-V)$ to range from 0 to 0.6 and stellar population ages ranging from 0 to 13 Gyr. Ilbert et al. (2010) provide a more detailed description of how the physical parameters are estimated.

We are able to determine stellar masses using *BRI* and K_s-band data for 454 of our selected galaxies. The *K*-band survey of the DEEP2 fields covers 60% of the area so *K*-band photometry is not available for all galaxies in the survey (Bundy et al. 2006). In order to test for systematic variation in the stellar mass determination for the remaining sample of galaxies with only *BRI* photometry, we compare the stellar masses for our 454 galaxies determined with *BRI* and K_s-band data with stellar masses determined for the same galaxies with just the *BRI* bands. The left panel of Figure 2 shows the comparison. The *x*-axis is the mass determination from *BRI* band data and the *y*-axis is the mass determination from *BRIK*$_s$-band data. The dashed line is the one-to-one correspondence and the solid line is a linear bisector fit to the data.

We perform a bootstrap linear fit by taking the bisector of the *X* versus *Y* and *Y* versus *X* regression using the routine *boot_xyfit.pro* from the IDL astronomy users library. Bootstrapping is a non-parametric statistical method of inferring errors whereby errors are calculated from the distribution of the fitted parameters for many fits to randomly selected subsample of the data. In order to minimize the covariance between the slope and intercept, we zero point the data by subtracting 10 from the logarithm of the stellar mass. The linear fit is given by

$$X_{BRIK_s} = (-0.042 \pm 0.006) - (1.00 \pm 0.01) X_{BRI}, \quad (2)$$

where $X_{BRI} = M_{BRI} - 10$, $X_{BRIK_s} = M_{BRIK_s} - 10$, and M_{BRI} and M_{BRIK_s} are the stellar masses determined by using three and four bands, respectively. The slope is consistent with unity. To first order, the absence of the K_S-band data results in only a ∼0.04 dex overestimate of the stellar mass.

The DEEP2 galaxies with K_s-band data from the full sample are generally brighter and more massive than our selected galaxies, while the color distribution is consistent with our selected sample. The K_s-band data for our selected sample span the full range of mass, color, and absolute *B*-band magnitude and the medians are 9.81, 0.68, and −20.7, respectively. To check for any systematic variations with galaxy properties, we fit half of the data that are below the median in mass, color, and magnitude, respectively, and find that the fits are all consistent

[2] http://www.cfht.hawaii.edu/∼arnouts/LEPHARE/cfht_lephare/lephare.html

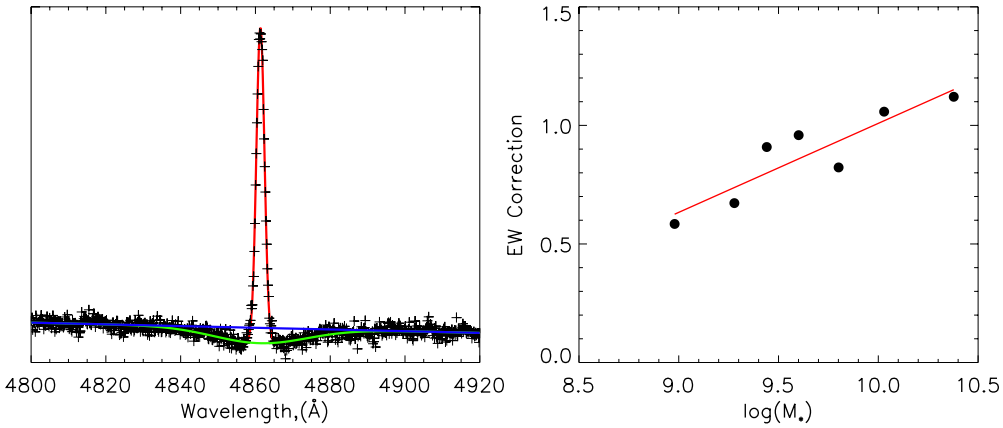

Figure 3. Left panel shows an example of a stacked spectrum. The red curve is a fit to the Hβ emission, the green curve is a fit to the Hβ absorption, and the blue line is a fit to the continuum. The area of the region bracketed by the absorption on the bottom, emission on the sides, and continuum at the top is the correction factor to the EW(Hβ). The right panel shows this correction for Hβ absorption as a function of stellar mass for data sorted into seven mass bins. The red line is a linear parameterization of the correction as a function of stellar mass.

(A color version of this figure is available in the online journal.)

within the errors. When K_s-band photometry is unavailable, we subtract 0.04 dex from the mass to correct for the systematic overestimate. After applying this correction, there is a 0.12 dex dispersion between the one-to-one correspondence of the two mass estimates.

We have redetermined the local MZ and LZ relations from ∼21,000 galaxies in the SDSS data release 7 (see the Appendix). We compared our stellar mass determination using Le Phare with those determined by the MPA/JHU team from fitting the photometry and a Kroupa IMF (Kroupa 2001). Both methods use stellar population synthesis to fit the photometry and we expect the estimates to only vary by a constant offset. The right panel of Figure 2 shows this comparison. The dashed line is the one-to-one correspondence and the solid line is a bootstrap linear bisector fit to the data as described earlier. The linear fit is given by

$$X_{\rm LP} = (0.198 \pm 0.001) + (1.035 \pm 0.003) X_{\rm SDSS}, \quad (3)$$

where $X_{\rm LP} = M_{\rm LP} - 10$ and $X_{\rm SDSS} = M_{\rm SDSS} - 10$. $M_{\rm LP}$ and $M_{\rm SDSS}$ are the stellar masses determined using Le Phare and those provided by the MPA/JHU team, respectively. As before, to minimize the covariance of the slope and intercept, we zero point the data by subtracting 10 from the masses. The slope is near unity and to first order the estimates differ by only a constant offset of 0.198 dex (a factor of ∼1.6). Taking into account this constant offset, there is a 0.14 dex dispersion in the one-to-one correspondence between the two mass estimates.

For local galaxies it has been shown that the errors between photometric and dynamical mass are typically ∼0.2 dex (Drory et al. 2004). In this study, we observe galaxies at $z \sim 0.8$ and therefore expect even greater errors in the photometric determination of mass. Moreover, Conroy et al. (2009) have shown that additional uncertainties in estimates of physical parameters from stellar population synthesis modeling result from the choice of IMF, dust model, and spectral libraries. However, the full impact of these effects on the absolute calibration of the physical parameters is still not well understood. Therefore, when investigating the evolution of the MZ relation, we take care to have a consistent relative calibration of the physical parameters between the samples. The absolute calibration remains uncertain.

3.2. Correction for Stellar Balmer Absorption

When measuring EWs, it is necessary to make a correction for underlying stellar absorption in the Balmer lines. Kobulnicky & Phillips (2003) have estimated an average correction of 2 Å in the EW(Hβ) for the underlying Balmer absorption using 22 galaxies from the spectroscopic galaxy atlas of Kennicutt (1992). The galaxies in the Kennicutt atlas have a spectral resolution of 5–8 Å. We expect the effects of Balmer absorption to be greater in galaxy spectra with lower resolution because the flux of the narrow emission line is spread over a broader region of the absorption trough. Presumably for this reason, Cowie & Barger (2008) find a correction of 1 Å by stacking spectra observed using DEIMOS onboard Keck with a spectral resolution of 3.5 Å. The DEEP2 data have also been obtained using DEIMOS but with a smaller spectral resolution of 1.4 Å.

Unfortunately, the low S/N in our data does not allow us to investigate the Balmer absorption in individual galaxy spectra. However, the strength of the Balmer absorption is a function of the age of the stellar population and is therefore expected to correlate with physical parameters of the galaxy such as stellar mass. In order to investigate the effects of stellar absorption on our measurement, we stack our spectra in bins of stellar mass and examine the effect of the Balmer absorption on the EW(Hβ).

We stack our spectra into seven mass bins. We normalize each spectrum to the continuum by dividing by the median value of the continuum between 4800–4815 Å and 4900–4915 Å. We then stack ∼230 spectra in each mass bin by interpolating all spectra to have the same wavelength vector and take the median of the flux corresponding to each wavelength element. We get similar results if we take the mean rather than the median. The left panel of Figure 3 shows an example of a stacked spectrum. We see that the Hβ emission line sits on a broad absorption trough. The EW(Hβ) correction accounts for the integrated flux of the emission line (red curve) that lies below the continuum (blue curve) and would not be included when measuring the EW(Hβ) in lower S/N spectra due to the absorption (green curve). To obtain a correction, we measure the EW(Hβ) for the stacked spectrum and a corrected spectrum with the absorption removed. The right panel shows the correction to the EW(Hβ) as a function of stellar mass. The red line is a linear least-squares

fit given by

$$\mathrm{EW_{corr}} = (1.01 \pm 0.05) + (0.38 \pm 0.08)\mathrm{x}, \quad (4)$$

where $x = \log(M_*) - 10$. $\mathrm{EW_{corr}}$ is the amount added to the EW(Hβ) to correct for underlying absorption. We emphasize that the correction given by Equation (4) is sensitive to the fitting procedure. A different method (using a smaller continuum window, for example) may yield a different correction. The median correction to the EW(Hβ) in our sample is 0.9. We note that this correction does not significantly affect our derived MZ relation owing to the fact that the median correction of 0.9 Å is small compared to the median EW(Hβ) of 12.1 Å. This small correction translates to a median increase of 0.04 dex in metallicity.

We perform a simple test in order to assess the effect of varying the spectral resolution on the Balmer absorption correction. We convolve our stacked spectra with Gaussians of varying widths. We find that the Balmer correction is sensitive to the spectral resolution. The correction increases with smaller spectral resolution and the slope of the correction with respect to stellar mass flattens. We speculate that the larger correction found by Kobulnicky & Phillips (2003) may be attributed to the lower spectral resolution of their data. In a future study, using higher quality data we hope to quantitatively establish the magnitude of this effect.

3.3. Metallicity Determination

We use the strong-line diagnostics of KK04 as presented in KE08 in order to obtain an estimate of galaxy gas-phase metallicities. The diagnostics are based on the Kewley & Dopita (2002) R_{23} theoretical calibrations. In both diagnostics, the metallicity is determined using the R_{23} and O_{32} ratios. We calculate these ratios from our EWs such that

$$R_{23} = \frac{\mathrm{EW([O\,II])} + \mathrm{EW([O\,III])}}{\mathrm{EW(H}\beta)} \quad (5)$$

and

$$O_{32} = \frac{\mathrm{EW([O\,III])}}{\mathrm{EW([O\,II])}}, \quad (6)$$

where EW([O II]) is for the [O II] doublet and EW([O III]) is taken to be 1.33 × EW([O III] λ5007). We have used the assumption that the ratio of the fluxes of [O III] λ5007 to [O III] λ4959 is 3 (Osterbrock 1989). We have fitted the [O III] λ4959 line because the widths of the Hβ, [O III] λ4959, and [O III] λ5007 line fits are tied in order to increase the S/N of the fit, as described in the Appendix, but the S/N in the EW([O III] λ5007) is higher and the EW([O III] λ4959) is inferred from theoretical considerations for the metallicity determination.

We use Equations (A4) and (A6) given in the Appendix of KE08 to derive the ionization parameter and metallicity, respectively. The R_{23} method for determining metallicities is known to be sensitive to the ionization parameter. The ionization parameter characterizes the ionization state of the gas and quantitatively represents the number of ionizing photons per second per unit area divided by the hydrogen density. The ionization parameter has the units of velocity and can be thought of as the maximum velocity of the ionization front through the nebula. The metallicity and ionization parameter are interdependent. In order to obtain a consistent measurement of the metallicity and ionization parameter an iterative scheme is used, the details of which are provided in the Appendix of KE08. Furthermore, all metallicities used in this study for comparison that are not explicitly calculated using the KK04 calibration are converted to be consistent using the conversions provided in KE08.

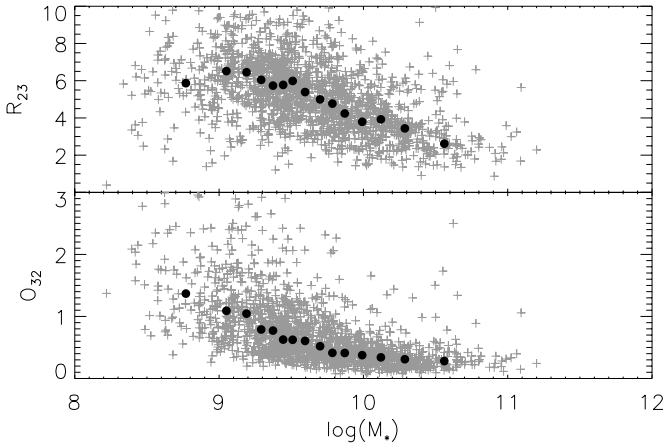

Figure 4. R_{23} (top) and O_{32} (bottom) line ratios as a function of stellar mass. The gray pluses are the unbinned data and the black filled circles are the data binned into 15 mass bins where each bin has equal number of data points.

Figure 4 shows the R_{23} (top) and O_{32} (bottom) line ratios for our sample. The gray pluses are the individual measurements and the black filled circles are the data sorted into 15 mass bins of equal number of data points. The median values of the R_{23} and O_{32} line ratios are 5.1 and 0.6 and median errors are 0.6 and 0.06, respectively. Both the R_{23} and O_{32} line ratios are sensitive to the metallicity and the relation between stellar mass and the line ratios can be attributed to the relation between stellar mass and metallicity.

Metallicity is not a monotonic function of R_{23}, but rather is doubly valued for a given ratio. A particular value of R_{23} corresponds to two different metallicities, one on the higher metallicity branch and one on the lower metallicity branch. The peak of the R_{23} ratio occurs at $12 + \log(\mathrm{O/H}) \approx 8.4$. This degeneracy is due to the fact that on the lower branch R_{23} scales with metallicity because the intensity of the collisionally excited [O II] and [O III] lines scales with the abundance. On the upper branch, nebular cooling, which results from collisional excitation followed by photon emission, effectively cools the nebula decreasing the electron temperature leading to a decrease in the rate of collisional excitation of the [O II] and [O III] lines. In order to break this degeneracy, generally other line ratios such as [N II]/H_α are used. However, in our sample, these lines are not observed and the metallicity is assumed to lie on the upper branch. This assumption breaks down at lower masses. Looking at the R_{23} mass relation in Figure 4, a turnover appears to occur at about $\log(M_*) \sim 9.2$ and we revisit this issue in Section 4.

4. MASS–METALLICITY AND LUMINOSITY–METALLICITY RELATIONS

From our measured EWs and photometry, we can estimate both the gas-phase oxygen abundances and stellar masses for the galaxies in our sample. From the Spearman rank test, we conclude with over 99% confidence that we have a positive correlation between mass and metallicity and luminosity and metallicity. This confidence in our observed correlation justifies a fit to the data.

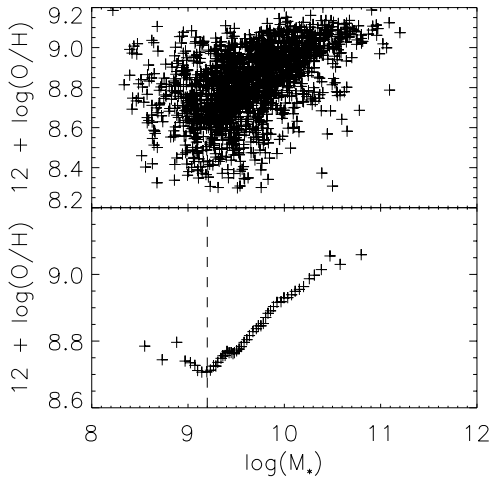

Figure 5. Mass and metallicity for the DEEP2 sample. The top panel shows the metallicity plotted against mass for the 1631 galaxies in our sample. The bottom panel is a boxcar averaged smoothing of the data displayed in the top panel binned by mass. We attribute the break in the slope at $M \sim 10^{9.2}\,M_{\odot}$ to the misplacement of galaxies on the upper branch of the KK04 metallicity diagnostic. The vertical dashed line ($M = 10^{9.2}\,M_{\odot}$) in the lower panel is our lower limit cutoff mass used in determining the MZ relation for the DEEP2 sample.

4.1. The Mass–Metallicity Relation

The top panel of Figure 5 shows stellar mass and metallicity measured for our sample of 1631 galaxies. The bottom panel shows binned data with a boxcar smoothing. In determining the metallicity, we have assumed that all galaxies fall on the upper branch of the KK04 metallicity diagnostic. T04 have shown that in the local universe the MZ relation extends down to a stellar mass of $M_* = 10^{8.5}\,M_{\odot}$ with no break in the slope. We work under the assumption that the MZ relation at $z \sim 0.8$ extends to at least $M_* \sim 10^9\,M_{\odot}$ with no break in slope. Under this assumption, we interpret the break in the slope at $M_* = 10^{9.2}\,M_{\odot}$ observed in the bottom panel of Figure 5 to be caused by the misplacement of lower branch galaxies on the upper branch. This turnover mass is further evidenced by the R_{23} ratio as a function of stellar mass seen in Figure 4. We take a lower mass limit, indicated by the vertical dashed line in the bottom panel of Figure 5, of $M_* = 10^{9.2}\,M_{\odot}$ to fit our MZ relation. We note that 283 of our 1631 galaxies fall below this limit, leaving us with 1348 galaxies from which we determine the MZ relation.

We parameterize the MZ relation with a quadratic function of the form

$$12 + \log(\mathrm{O/H}) = \mathrm{A} + \mathrm{Bx} + \mathrm{Cx}^2, \quad (7)$$

where $x = \log(M_*) - 10$. Our data and fit residuals are not normally distributed so we apply a standard non-parametric bootstrapping technique in determining the fit parameters and errors. One of the underlying assumptions of the bootstrapping method is that the observed distribution reasonably approximates the parent distribution. Under this assumption and the assumption of independence of the sample, properties determined from many independent random subsamples of the data should be normally distributed. We begin by randomly selecting, with replacement, 1348 galaxies from our sample of 1348 galaxies. Meaning, within a random subsample some data points may be selected more than once while others may not be selected at all. We then bin these randomly selected galaxies by sorting them into 15 equally populated mass bins. The mass and metallicity in each bin are determined by taking the median of the data in the bin. We perform a least-squares quadratic fit to the binned data using the routine *poly_fit.pro* in IDL. We randomly resample and fit the data 10,000 times and take the mean and standard deviation of this distribution of fitted parameters, which are normally distributed, as the fit parameters and errors for the MZ relation.

The MZ relation is best fitted by

$$12 + \log(\mathrm{O/H}) = 8.923 + 0.24\,\mathrm{x} - 0.06\,\mathrm{x}^2, \quad (8)$$

with the 1σ errors in each of the parameters in Equation (8) given by $\sigma_A = 0.007, \sigma_B = 0.01$, and $\sigma_C = 0.03$. Figure 6 shows the DEEP2 MZ relation at $z \sim 0.8$ compared to the local MZ relation from SDSS (see the Appendix). The black filled circles are the data sorted into 15 mass bins. Each bin contains ~90 data points and the errors on the data are determined by randomly selecting ~90 data points in each bin and taking the median of the subsample. We take the standard deviation of this distribution as the error in each bin. We note that this scatter characterizes the distribution of metallicities within each mass bin and therefore accounts for both measurement uncertainties and intrinsic scatter in the metallicity determination. The gray lines are the 16% and 84% percentile contours of the data. The large dispersion at the high-mass end is due to the large interval in mass covered by the highest mass bins.

Overall, we find that the high-mass ($M > 10^{10.5}\,M_{\odot}$) DEEP2 galaxies have similar metallicities (within the errors of ± 0.05 dex) to local galaxies at the same stellar mass. At lower masses ($M < 10^{10.5}\,M_{\odot}$), the DEEP2 galaxies have lower metallicities than the SDSS sample for a given stellar mass, up to a $\Delta \log(\mathrm{O/H}) \sim 0.15$ dex.

4.2. The Luminosity–Metallicity Relation

Figure 7 shows the LZ relation derived from the DEEP2 sample and the local sample from SDSS. Similar to the MZ relation, the LZ relation is determined for galaxies with $M_* > 10^{9.2}\,M_{\odot}$. The filled circles are the median metallicities in 15 luminosity bins. The solid curve is a linear fit to the binned data and is parameterized by the equation

$$12 + \log(\mathrm{O/H}) = (8.909 \pm 0.006) - (0.117 \pm 0.008)\mathrm{X_B}, \quad (9)$$

where $X_B = M_B + 21$. The errors in the fit and binned data of the LZ relation are derived in the same manner as for the MZ relation. The gray lines are the 16% and 84% percentile contours of the data. The dashed curve is the local LZ relation from SDSS taken from the Appendix of this paper. The fit made is over the full range of magnitudes ($-21 < M_B < -18$) of the local LZ relation. However, the local LZ relation appears to turn over at $M_B < -20$. The dot-dashed curve is a fit to the linear part of the local LZ relation with $M_B > -20$. The slope of this fit and the DEEP2 LZ relation are consistent to within the errors. KK04 find that the slope of the LZ relation for $z = 0.6$–0.8 and $z = 0.8$–1.0 is -0.117 ± 0.017 and -0.134 ± 0.032, respectively. To within the errors, the slopes derived by KK04 agree with DEEP2 and local LZ relation slopes as well.

5. DISCUSSION

In this section, we will discuss our key assumptions (Section 5.1), the evolution of the *B*-band luminosity as a function of stellar mass in the population of blue galaxies (Section 5.2) and compare our determination of the MZ relation with other authors (Section 5.3).

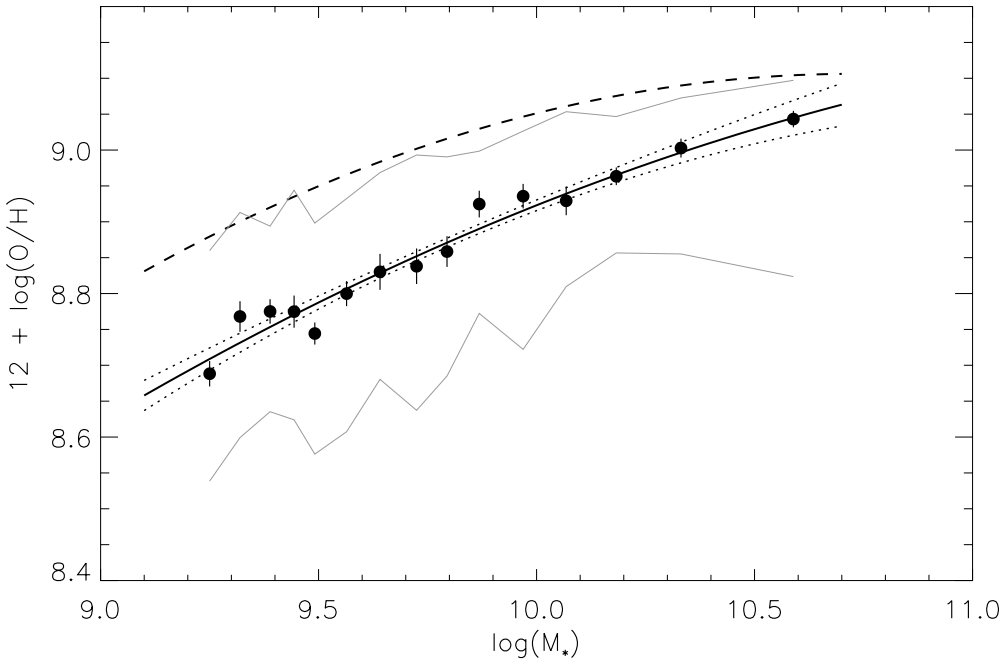

Figure 6. MZ relation derived from the DEEP2 sample. The black data points are the median of the mass and metallicity sorted into 15 bins. The bootstrapped errors are determined by randomly selecting galaxies from within each mass bin and determining the median for this subsample. The error bar then is the standard deviation of the distribution of median values. The gray lines are the 16% and 84% contours of the data. The solid curve is a quadratic fit to the data and the dotted curves around the quadratic fit are the 1σ uncertainty in the fit determined from bootstrapping the errors. The dashed curve is the local MZ relation from the Appendix of this paper.

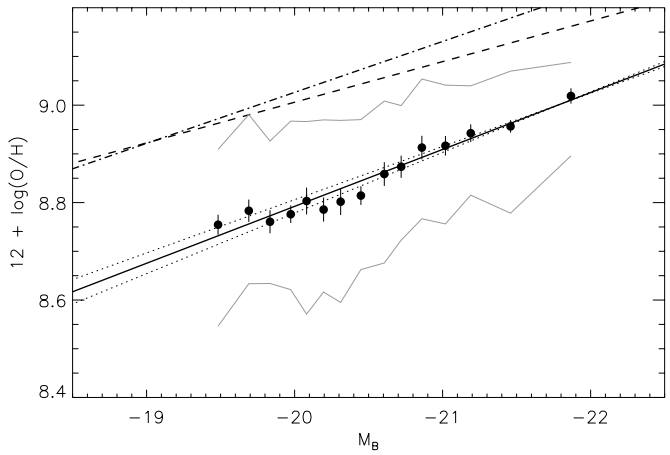

Figure 7. LZ relation derived from the DEEP2 sample. The black data points are the median of the M_B and metallicity sorted into 15 luminosity bins. The solid line is a linear fit to the data and the dotted lines are the 1σ uncertainty of the fit determined from bootstrapping errors. The gray lines are the 16% and 84% percentile contours of the data. The dashed line is the local LZ relation fit over the full range of magnitudes ($-21 < M_B < -18$). The local LZ relation appears to turn over for brighter galaxies and the dot-dashed line is a fit to the linear part of the relation ($M_B > -20$). See the Appendix of this paper for more details.

5.1. Assumptions

We list and address some key assumptions made in this paper.

1. All galaxies with $M_* \geqslant 10^{9.2}\,M_\odot$ are on the upper branch of the R_{23} diagnostic. At the lower mass end of the DEEP2 MZ relation, the dispersion is small and consistent with the dispersion found in the local MZ relation (T04). This small dispersion suggests that at $z \sim 0.8$, the vast majority of galaxies with $M_* > 10^{9.2}\,M_\odot$ are on the upper metallicity branch of the R_{23} diagnostic. Additionally, T04 have observed a continuous slope down to $M_* \sim 10^{8.5}\,M_\odot$. A breakdown of this assumption would result in the R_{23} measure of metallicity in low-metallicity galaxies to be significantly overestimated ($\sim$1 dex) resulting in a flattening of the MZ relation at lower masses. This flattening is observed to occur at $M_* = 10^{9.2}\,M_\odot$ and given the small dispersion, we hypothesize that misplacement on the upper branch is minor above this mass. Near-infrared spectroscopy to obtain additional line ratios for a representative subsample of DEEP2 galaxies is needed to test this hypothesis.
2. Metals are instantaneously recycled. This approximation was first introduced by Schmidt (1963). The approximation is valid when metals produced in massive stars, such as oxygen, are considered and if the star formation rate (SFR) is not subject to extreme variations on short timescale (Pagel 1997). From their study of DEEP2 galaxies since $z = 1.1$, Noeske et al. (2007b) determine that the dominant form of evolution is a gradual decline in star formation.
3. We have attempted to remove AGN using empirical limits on the R_{23} ratio and the color bimodality. This removes most of the galaxies whose emission is dominated by AGN, but composite galaxies in our sample may be blue and not exceed the empirical R_{23} limit. AGN contamination in composite galaxy spectra increases the R_{23} ratio due to the high [O III]/Hβ ratio. On the upper metallicity branch of the R_{23} diagnostic, the metallicity is a monotonically decreasing function of R_{23}. Therefore, AGN contamination will lower the metallicity estimate. However, due to their relatively small numbers in the DEEP2 blue galaxy sample (Weiner et al. 2007) and the small dispersion in the MZ relation, AGN contamination is likely to play a minor role in the MZ relation (Lamareille et al. 2009). Near-infrared spectroscopy to obtain additional AGN-sensitive emission-line ratios is required to verify this assumption.

4. Since its introduction by Salpeter (1955), the initial stellar mass function (IMF)—describing the mass distribution of stars at birth—has largely been taken to be universal and invariant. Indirect evidences for variations in the local IMF have been provided by the comparison of Hα emission to the far-ultraviolet flux (Meurer et al. 2009) and the Hα flux to broadband color index (Hoversten & Glazebrook 2008). Comparison of the rate of luminosity evolution to that of color evolution provides indirect observational evidence for a possible redshift evolution in the IMF (van Dokkum 2008). Furthermore, IMF variations have been cited as the possible cause of the MZ relation (Köppen et al. 2007). We work under the assumption that the IMF is universal.
5. MZ and LZ relation studies assume that the absence of low surface brightness galaxies (LSBGs) does not significantly bias the determination of the MZ and LZ relations. Impey & Bothun (1997) point out that LSBGs will be absent in magnitude-limited surveys. However, by comparing photometry in overlapping fields where both CFHT and *Hubble Space Telescope* imaging is available, no galaxies brighter than the magnitude limit of $R_{\rm AB} = 24.1$ are found to be lost due to low surface brightness (Simard et al. 2002; Willmer et al. 2006). Melbourne et al. (2007) come to similar conclusions regarding the loss of LSBGs from deep imaging in the GOODS-N field.

5.2. *B*-band Luminosity Evolution

In many previous studies, luminosity has been taken as a proxy for mass (Kobulnicky & Koo 2000; Pettini et al. 2001; Garnett 2002; Kobulnicky et al. 2003; Kobulnicky & Kewley 2004; Maier et al. 2004; Shapley et al. 2004, 2005). However, it has been recognized that the evolution in the LZ relation cannot straightforwardly be attributed to metallicity evolution, but that luminosity evolution must also be considered. By comparing Figures 6 and 7, we see that the offset in metallicity in the MZ relation is significantly smaller than the offset in the LZ relation. Lamareille et al. (2009; among others) suggest that the differential evolution in the LZ and MZ relations results from an evolution in the mass-to-light ratio. They estimate the evolution such that

$$\Delta M_B = a^{-1} \times [\Delta \log(\mathrm{O/H})^{\mathrm{M}} - \Delta \log(\mathrm{O/H})^{\mathrm{L}}], \quad (10)$$

where a is the slope of the LZ relation and $\Delta \log(\mathrm{O/H})^{\mathrm{M}}$ and $\Delta \log(\mathrm{O/H})^{\mathrm{L}}$ are the differences in metallicity at a fixed stellar mass and fixed B-band magnitude in the MZ and LZ relations, respectively. Equation (10) assumes that the metallicity evolution is characterized by the MZ relation and that additional evolution inferred from the LZ relation is due to evolution of the luminosity.

We estimate the evolution of the B-band luminosity as a function of stellar mass from Equation (10). We take the difference between the local and DEEP2 LZ relation, $\Delta \log(\mathrm{O/H})^{\mathrm{L}}$, to be the average difference between the binned DEEP2 data and the fit to the local LZ relation over all magnitudes (see Figure 7). Consequently, $\Delta \log(\mathrm{O/H})^{\mathrm{L}} = 0.20 \pm 0.03$ dex and $a = -0.11$. We take $\Delta \log(\mathrm{O/H})^{\mathrm{M}}$ to be the difference between the DEEP2 binned data and local MZ relation fit. The difference is parameterized by

$$\Delta \log(\mathrm{O/H})^{\mathrm{M}} = (0.12 \pm 0.01) - (0.08 \pm 0.02)\mathrm{x}, \quad (11)$$

where $x = \log(M_*) - 10$. Here we have performed a linear least-squares fit using *poly_fit.pro* and the errors are determined from the residuals of the fit and do not account for observational uncertainties.

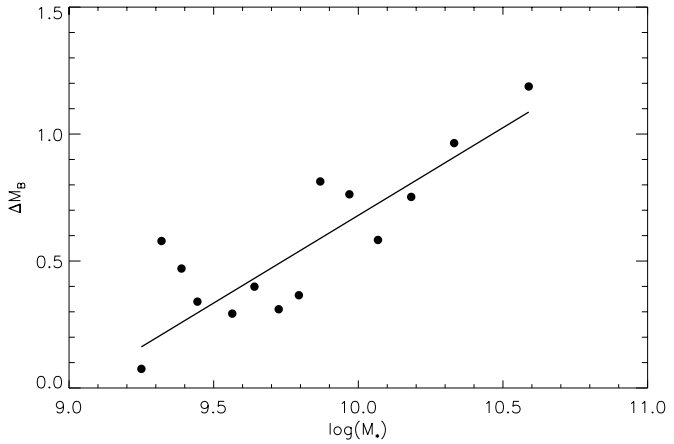

Figure 8. *B*-band luminosity evolution inferred from the comparison of our MZ and LZ relations. The black data points are determined by taking the difference between the binned DEEP2 data and the fit to the local MZ relation and plugging it into Equation (10). The line is from combining Equations (10) and (11).

Figure 8 shows the B-band luminosity evolution inferred from our comparison of the DEEP2 MZ and LZ relations. Combining Equations (10) and (11), we get

$$\Delta M_B = (0.68 \pm 0.06) + (0.7 \pm 0.1)\mathrm{x}, \quad (12)$$

the B-band luminosity evolution of blue star-forming galaxies between $z \sim 0.8$ and the local galaxy population as a function of stellar mass. This is shown in Figure 8 by the solid line.

It has been shown that the luminosity functions of blue galaxies evolve with time (Ilbert et al. 2005; Blanton 2006; Willmer et al. 2006; Faber et al. 2007). These studies conclude that M_B^* has dimmed by $\sim$1 mag since $z \sim 0.8$, consistent with the evolution observed in our sample at the higher stellar mass end. A differential evolution in the B-band Tully–Fisher relation has also been observed since $z \sim 1$ and is consistent with the observed luminosity evolution (Weiner et al. 2006). Noeske et al. (2007b) show that the star formation as a whole was higher at $z \sim 1$ and that the SFR gradually declines with galaxies spending 67% of their lifetime since $z = 1$ with SFR that are within a factor of two of their average and 95% of their time within a factor of four. In an accompanying letter, Noeske et al. (2007a) find that initial onset and rate of decline in star formation are functions of redshift and galaxy mass with less massive galaxies having later initial onsets with a lower rate of decline and consider this an important component of downsizing (Cowie et al. 1996). The absolute B-band luminosity is a tracer of star formation and the observed differential evolution with respect to stellar mass shown in Figure 8 may be attributed to this type of downsizing.

5.3. Comparison of MZ Relations

There are considerable difficulties in making a comparison of the MZ relation owing to the varying quality and type of data and the different methodologies and sample selections. The systematic differences among strong-line metallicity calibrations have been investigated by KE08. They derived conversions that reach agreement among calibrations to within ± 0.05 dex in metallicity. KE08 conclude that while absolute metallicity values are uncertain, relative metallicities (such as MZ relations) can be reliably compared, providing that the metallicities have been converted into the same base calibration.

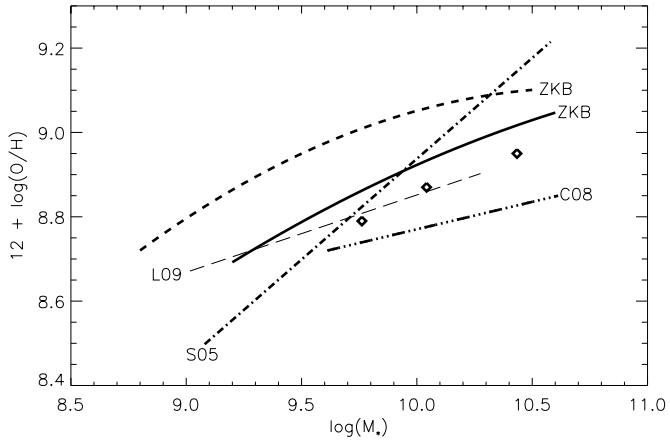

Figure 9. Comparison of the MZ relation derived by several authors. The solid line in this figure is our MZ relation derived for galaxies with $z = 0.75$–0.82 (labeled ZKB). The short dashed curve is the local MZ relation for galaxies with $z = 0.04$–0.1 from the Appendix of this paper (labeled ZKB). The long dashed curve is the MZ relation for galaxies with $z = 0.6$–0.8 (Lamareille et al. 2009, labeled L09). The dot-dashed curve is for galaxies with $z = 0.4$–0.98 (Savaglio et al. 2005, labeled S05). The triple-dot-dashed curve is for galaxies with $z = 0.475$–0.9 (Cowie & Barger 2008, labeled C08). The diamonds are the median instead of the mean of the data from Cowie & Barger (2008). Metallicities and masses have been converted to be consistent among the samples. The relations only cover the stellar mass range over which they were determined.

Though offsets between different metallicity calibrations can now be removed, the systematic effects on differing measurements of stellar mass have yet to be fully explored. Moreover, comparisons between spectral and photometric methods have not been rigorously investigated and the systematic effects of the photometric bands used in determining stellar mass remain uncertain. These problems are further compounded by the fact that many of the selection criteria in these studies may be a function of redshift (i.e., S/N of flux or EW, minimum values of flux or EW, color, etc.) and therefore the samples from which the MZ relations are determined may not be comparable even if similar selections are used.

Several authors have investigated the MZ relation covering the redshift interval examined in this study ($z = 0.75$–0.82). Figure 9 compares our MZ relation (solid curve) with previously derived relations from Savaglio et al. (2005; dot-dashed), Cowie & Barger (2008; triple-dot-dashed), and Lamareille et al. (2009; long dashed line). All metallicities have been converted to the KK04 calibration using the conversions in KE08. We have attempted to make the stellar masses consistent with ours by converting all the determinations to the Chabrier IMF used in this study. The relations plotted only cover the stellar mass range over which they were determined.

The first attempt to investigate the MZ relation at intermediate redshifts was made by Savaglio et al. (2005) using the Gemini Deep Deep Survey. This sample consists of 28 galaxies from the Gemini Deep Deep Survey with emission in [O II], Hβ, and [O III] at the 3σ level covering the redshift range of $z = 0.40$–0.98. This sample consists of galaxies designated as late (7/28) and intermediate type (21/28). This sample is augmented with 28 galaxies from the Canada France Redshift Survey (Lilly et al. 1995). The dot-dashed fit in Figure 9 is a linear bisector fit of the S05 mass and metallicity. Though Savaglio et al. establish an MZ relation at higher redshifts, the small sample size and selection in addition to the fitting method do not allow us to make a direct comparison with our determination.

Lamareille et al. (2009) study the evolution of the MZ relation by splitting their sample into three redshift ranges. They find that the most massive galaxies undergo the most evolution at $z \sim 0.8$, implying that the slope of the MZ relation flattens out at higher redshifts. However, L09 do not find a strong Spearman rank correlation coefficient, thus hindering a rigorous statistical analysis. The relation shown in Figure 9 (long-dashed line) is a linear fit to average metallicities in four mass bins for ~130 galaxies in the redshift range of $z = 0.6$–0.8. The galaxies are selected to have S/N > 4 in the flux of the [O II], Hβ, and [O III] emission lines. The flattening of the slope at higher redshifts may possibly be a consequence of the S/N cut on the [O II] and [O III] lines. These cuts may be a function of redshift and bias against higher metallicity galaxies generally found at higher stellar masses. At lower masses, the MZ relation of L09 is in agreement with our determination.

Cowie & Barger (2008, hereafter C08) study the evolution of the MZ relation by splitting their sample into a low-z and mid-z redshift interval. The two intervals are $0.05 < z < 0.475$ and $0.475 < z < 0.9$ and have a median redshift of 0.44 and 0.75, respectively. The low-z and mid-z samples have 35 and 154 galaxies, respectively. They find that there is a 0.25 dex difference in the metallicity in the mid-z sample as compared with the local relation and that the metallicity increases by 0.13 dex between the mid-z and low-z sample. The triple-dot-dashed line in Figure 9 shows the mid-z relation.

A major source of discrepancy between our determination and C08 can be attributed to the fitting procedure. Figure 31 of C08 shows that the spread in metallicity becomes larger as metallicity decreases. This may result from the greater uncertainty in determining metallicity from the R_{23} diagnostic which becomes less sensitive to metallicity around the R_{23} local maximum ($12 + \log(\mathrm{O/H}) \sim 8.4$; see C08, Figure 23; or KK04, Figure 7, for example). The relation is curved so symmetric errors in R_{23} become asymmetric errors in metallicity. In a least-squares fit, the data are assumed to be normally distributed, however, in this case they are not and outliers exert greater influence in determining the best fit. Looking at Figure 63 of C08 shows that the median of the metallicity in four mass bins is systematically higher than the fitted relation. With the diamonds in Figure 9, we plot the median of the MZ relation for the mid-z sample sorted into three mass bins (L. Cowie 2010, private communication). We fit our relation to the median metallicity in 15 mass bins as described in Section 4. The MZ relation determined from the median of the C08 data is more comparable to our determination. Given the many uncertainties discussed in comparing the MZ relation, the agreement between the relation of L09, C08, and our determination from DEEP2 is promising.

Our MZ relation comparisons highlight the need for consistent sample selection and MZ relation fitting techniques when comparing MZ relations at the same or different redshifts.

6. SUMMARY

We have conducted a study of the MZ and LZ relations at $z \sim 0.8$ using the 1348 galaxies from the DEEP2 survey. This large sample has allowed us to establish the MZ and LZ relations at $z \sim 0.8$ with greater statistical significance than previous studies in this redshift regime. Such a large sample within a small redshift range is essential for avoiding evolution effects in luminosity or metallicity that may influence LZ and MZ relations derived over a larger redshift interval.

We have obtained stellar masses by inferring an SED from our photometry and fitting it with current stellar population

synthesis models. We have determined the gas-phase oxygen abundance in a consistent manner from strong-line methods. We summarize our main results as follows.

1. We find a clear correlation between mass and metallicity at $z \sim 0.8$, consistent with previous work (Savaglio et al. 2005; Cowie & Barger 2008; Lamareille et al. 2009). The level of chemical enrichment achieved by galaxies is a function of stellar mass. At $z \sim 0.8$, galaxies with $M_* \sim 10^{10.6} M_\odot$ have metallicities that are lower by 0.05 dex as compared to the local sample, which is within the errors of the metallicity calibration conversions. The metallicity difference between $z \sim 0.8$ and local galaxies rises to 0.15 dex at $M_* \sim 10^{9.2} M_\odot$.
2. There is a clear correlation between luminosity and metallicity at $z \sim 0.8$, as shown in previous work. The level of chemical enrichment achieved by galaxies is a function of luminosity. The metallicity at a given luminosity at $z \sim 0.8$ is 0.20 dex lower than the local sample due to the combination of metallicity and luminosity evolution with redshift.
3. The offset in the LZ relation between $z \sim 0.8$ and local galaxies is significantly larger than the offset observed in the MZ relation between these two redshifts. We attribute this difference to evolution in the mass-to-light ratio between $z \sim 0.8$ and $z \sim 0$. We infer a luminosity evolution that scales with stellar mass and is consistent with determinations from studies of blue galaxy luminosity functions.
   Both the luminosity and metallicity evolution are a function of stellar mass, consistent with the downsizing scenario of galaxy evolution.

In a subsequent paper, we will examine the origin of the MZ relation and its evolution over cosmological timescales.

We thank the referee Ben Weiner for his careful reading and many useful suggestions for improving the paper. L. Kewley and J. Zahid gratefully acknowledge support by NSF Early Career Award AST07-48559. We thank the DEEP2 team for making their data publicly available. The analysis pipeline used to reduce the DEIMOS data was developed at UC Berkeley with support from NSF grant AST-0071048. We also thank Kevin Bundy for generously sharing his *K*-band photometry and Christy Tremonti for making her measurements available. We are grateful to Stephane Arnout and Olivier Ilbert for making their photo-z code available for use in estimating galaxy stellar mass and are thankful to Olivier Ilbert and C. J. Ma for help in installing and implementing Le Phare. Finally, we thank Charlie Conroy, Christy Tremonti, Kristian Finlator, Len Cowie, David Rupke, Dave Sanders, Chiaki Kobayashi, Ezequiel Treister and TC (the player), and Josh Barnes for useful discussion. We acknowledge the cultural significance Mauna Kea has for the Hawaiian community and with all due respect say mahalo for its use in this work.

APPENDIX

A.1. Line Fitting and Line Ratio Determination

Conventionally, when spectra are not flux calibrated, as is the case in most spectroscopic redshift surveys, EWs are utilized in determining the emission-line ratios used for inferring metallicity (Kobulnicky & Phillips 2003, hereafter KP03). The essential feature of EWs is the normalization of the line emission to the underlying continuum. Here we will discuss the algorithm developed to determine line ratios in a self-consistent manner.

We define $F(x)$ as the flux vector of our spectra with x being the rest-frame wavelength vector corresponding to each resolution element. We mask out $\pm 5\sigma_v$ of our rest-frame line center wavelengths (from NIST[3]) and fit a global continuum. Here we take σ_v to be a velocity dispersion of 150 km s^{-1}. We model the global continuum as

$$C(x) = \sum_{i=1}^{39} c_i T_i(x) + \sum_{j=0}^{2} p_j x^j, \tag{A1}$$

where $T_i(x)$ are the model stellar spectra obtained from Bruzual & Charlot (2003). We perform a bounded value nonlinear least-squares fit using the MPFIT[4] set of routines (Markwardt 2009) in IDL to obtain c_i and p_j with the constraint that $c_i \geqslant 0$. We obtain a continuum-normalized flux, such that

$$N(x) = \frac{F(x)}{C(x)} - 1, \tag{A2}$$

and fit a three-parameter Gaussian, $A_N e^{-\frac{(x-x_N)^2}{2\sigma_N}}$ to all emission lines. A_N, x_N, and σ_N are the gain, line center, and sigma of the Gaussian, respectively, and are used as initial estimates for fits to the local flux. In all our fits to the DEEP2 data, we derive the errors on our parameters by propagating the measurement uncertainties in the spectrum.

We define $L(x)$ as the local flux for each line. $L(x) = F(x)$ in the range $x_N - 25\sigma_N < x < x_N + 25\sigma_N$ and zero elsewhere. We perform a bounded value nonlinear least-squares fit to the local flux $L(x)$ with a two-component model $r(x)$, such that $r(x) = p(x) + g(x)$, where

$$p(x) = a + bx \tag{A3}$$

is a linear fit that models the underlying continuum and

$$g(x) = \sum_{i=1}^{n} a_i e^{\frac{(x-x_{oi})^2}{2\sigma^2}} \tag{A4}$$

is a Gaussian that models the emission line, where a_L, x_{oL}, and σ_L are defined as the gain, center, and sigma of the Gaussian fit to $L(x)$, respectively. We note that in the case of Hβ, due to possible underlying stellar absorption, we fit continuum between 4775–4815 Å and 4905–4945 Å. It should be noted that σ in Equation (A4) does not have a summation index. If $n > 1$, then the multiple Gaussians simultaneously fitted will have different a_L and x_{oL} but the same σ_L. The parameters of the Gaussian are constrained such that $a_L \geqslant 0$, x_{oL} can only vary by ± 2 Å from the line centers obtained from NIST[5] and 0 Å $< \sigma_L <$ 10 Å. For the [O II] $\lambda\lambda$3726, 3728 doublet $n = 2$ and for all other lines $n = 1$. This enables us to fit the local continuum, $p(x)$, to all lines separately, except in the case of the [O II] doublet where we fit the continuum to both lines simultaneously.

We obtain a continuum-normalized local flux, $R(x)$, such that

$$R(x) = \frac{L(x)}{p(x)} - 1. \tag{A5}$$

[3] National Institute of Standards and Technologies.
[4] http://purl.com/net/mpfit
[5] This is done to account for possible errors in the redshift determination, reported line centers from NIST and/or wavelength calibrations.

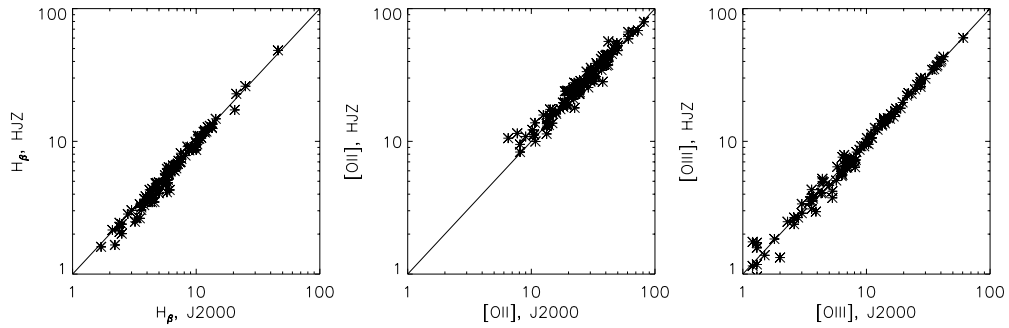

Figure 10. Comparison of fitted emission-line pseudo-EWs (denoted "HJZ," *y*-axis) to the reported EWs (denoted "J2000," *x*-axis) for 102 galaxies from the Nearby Field Galaxies Survey (Jansen et al. 2000). From left to right, the plots show the H_β, [O II], and [O III] comparisons, respectively. The solid line in each plot shows the one-to-one agreement.

We refit a model, $g_R(x)$, of the form given in Equation (A4) with $n = 3$ for the H_β and [O III] λλ4959, 5007 lines and $n = 2$ for the [O II] λλ3726, 3728 doublet. These values of n for the two sets of lines ensure that the fitted σ will be the same for all lines in the set. We obtain a pseudo-EW for each line, EW_p, such that $EW_p = a_R\sigma_R\sqrt{2\pi}$, where a_R and σ_R are the parameters from the fit of $g_R(x)$ to $R(x)$.

It becomes problematic to measure an EW or pseudo-EW when the S/N is low in the underlying continuum. In this situation, the continuum is poorly measured and therefore a normalization to the continuum is prone to large errors. Before normalizing the local flux, $L(x)$, to the continuum, $p(x)$, we estimate the noise of the local continuum, σ_c, by taking the rms of $C'(x)$, where $C'(x) = L(x) - r(x)$. We require that $p(x)$, in the region of the line $x_o - 3\sigma_L < x < x_o + 3\sigma_L$, be $1\sigma_c$ above zero. If this condition is not met, we do not normalize to the continuum but instead fit a function of the form given in Equation (A4) to $D(x)$, where $D(x) = L(x) - p(x)$. We then calculate a pseudo-EW from the parameters of the fit. In this study, a small fraction (∼1%) of our Galaxies have such a low S/N in the continuum and are excluded from the study.

A.2. Comparison of Line Ratio Determination

In order to test the robustness of our fitting method, we compare our pseudo-EW and line ratios with published EWs and line ratios determined from calibrated fluxes from the Nearby Field Galaxies Survey (NFGS; Jansen et al. 2000). KP03 compare how well interactively determined EW ratios correspond to those determined from measured fluxes. We deredden the fluxes from NFGS sample as described in KP03 and use their results as a benchmark for comparison. Of the 198 galaxies in the survey, 118 have published fluxes. Of those 118, 104 galaxies have an S/N of at least 8 for [O II] λλ3726, 3728, [O III] λλ4959, 5007, and H_β emission lines. We remove two additional galaxies that have a good fit determined visually but poor agreement with ratios determined from calibrated fluxes, presumably due to the underlying continuum which is poorly measured, leaving us with a sample of 102 galaxies plotted in Figures 10 and 11.

Figure 10 shows a direct comparison between the EWs determined by Jansen et al. (2000) and the pseudo-EW determined by our automated method. The rms dispersion from one-to-one agreement is 0.6, 4.0, and 0.7 Å with the mean value of the EW being 7.5, 28.0, and 15.3 Å for H_β, [O II], and [O III], respectively.

In order to justify the fact that the pseudo-EW can be used in inferring gas-phase metallicities, we need to establish agreement between the calibrated flux ratios and our pseudo-EW ratios. Figure 11 shows agreement in line ratios determined with our method as compared to those from calibrated fluxes with an rms dispersion from one-to-one agreement of 0.10, 0.06, 0.11, and 0.08 dex for the [O II]/H_β, [O III]/H_β, O_{32} and R_{23} ratios, respectively. Table 3 gives the rms deviation from one-to-one agreement between line ratios determined using the two different methods. The top row shows the rms deviation from KP03 and the bottom row shows the rms deviation for our automated method for our sample of 102 galaxies. The median absolute deviation between the EW and flux-calibrated metallicities is <0.01 dex. In this local sample, the errors from the statistical measurement uncertainties are about one half of those introduced by using EWs or our pseudo-EW in line ratio determinations. Because galaxies are fainter at higher redshift, we expect them to have larger measurement uncertainties, thereby making the errors from using EWs comparable or even less than the statistical measurement uncertainties.

Table 3
rms Deviation Between Pseudo-EW and Flux-calibrated Line Ratios

	[O II]/H_β (dex)	[O III]/H_β (dex)	O_{32} (dex)	R_{23} (dex)
KP03	0.11	0.05	0.12	0.08
HJZ	0.10	0.06	0.12	0.08

Notes. rms deviation comparison of one-to-one agreement between pseudo-EW and flux-calibrated line ratios from Kobulnicky & Phillips (2003; top row) and our automated method (bottom row).

The O_{32} and R_{23} ratios are of particular importance because of their use in inferring metallicities. Figure 11 and Table 3 demonstrate that our method for determining line ratios is comparable to those that use flux-calibrated ratios. Figure 12 shows a typical spectrum and fit used in this study from the DEEP2 survey. Our automated method has several advantages over interactive determination of EWs. (1) The method is automated so considerably faster than interactively determining EWs and much more practical when working with large samples. (2) The automated method yields results that are reproducible because it no longer requires the input of wavelength limits in determining EWs. (3) The measurement errors in flux, when available, can be propagated through to the determination of metallicity and therefore provide a much more robust estimate of the true errors in 12 + log[O/H]. (4) In data where a low S/N makes it difficult to distinguish between the line and the continuum, the automatic fit is less susceptible to confusion. (5) Low S/N spectra where the continuum is not detected, EWs cannot be determined. These cases are handled in a much more

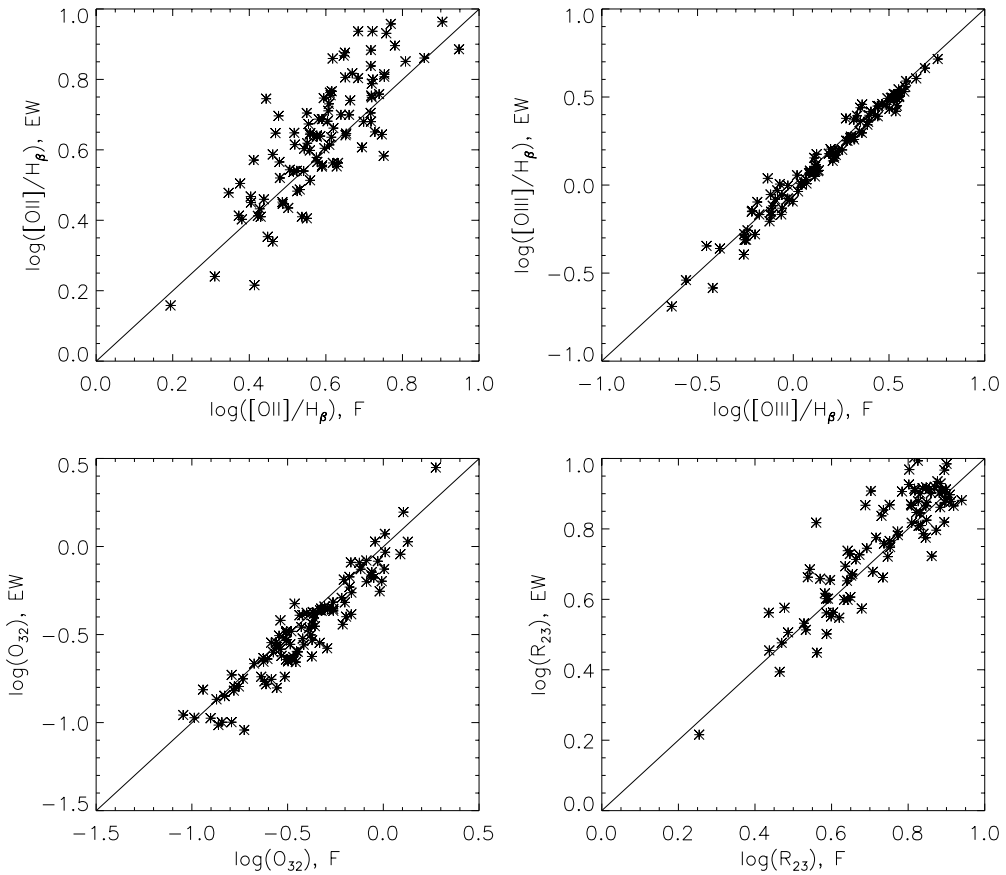

Figure 11. Comparison of fitted emission-line pseudo-EW ratios (denoted "EW," *y*-axis) to dereddened emission-line flux ratios (denoted "F," *x*-axis) for 102 galaxies from the Nearby Field Galaxies Survey (Jansen et al. 2000). From the top left panel going clockwise, we show the [O II]/H_β, [O III]/H_β, R_{23} and O_{32} ratios, respectively. The solid line in each panel shows the one-to-one agreement between the two methods.

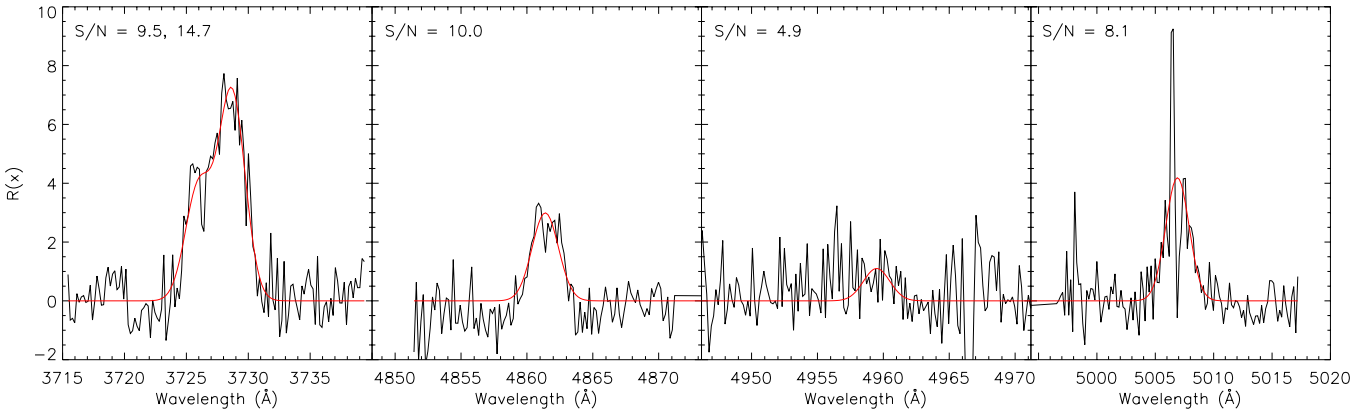

Figure 12. Typical spectra from the DEEP2 survey with an S/N EW(H_β) equal to our median value of 10.0. From left to right, the spectra (black curve) and Gaussian fit (red curve) for [O II] λλ3726, 3728, H_β, [O III] λ4959, and [O III]λ5007. The S/N for each spectrum is displayed. The underlying Balmer absorption can be seen in the fit to Hβ.

(A color version of this figure is available in the online journal.)

robust manner allowing us to measure a pseudo-EW even when EWs cannot be measured.

A.3. Redetermined Local MZ and LZ Relations from SDSS

The local MZ relation has been determined from the SDSS data by both T04 and KE08. T04 derive a galaxy averaged gas-phase metallicity by simultaneously fitting the most prominent emission lines with stellar population synthesis and photoionization models. KE08 determine the metallicity using several common strong-line diagnostics and calibrations and provide conversions between the various methods. Additionally, they investigate the effects of various AGN classification scheme and aperture covering fraction. The two determinations differ by as much as 0.3 dex when compared directly due mainly to the difference in methodology of determining metallicities. Converting to the same metallicity diagnostic using Table 3 from KE08 the difference decreases to <0.05 dex.

The different MZ relations found in the literature at various redshifts may not necessarily be directly comparable. The

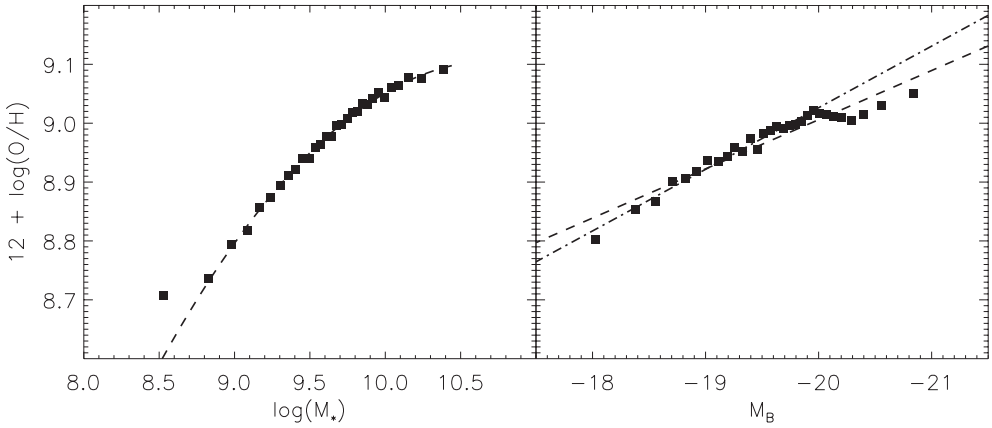

Figure 13. Local MZ (left) and LZ (right) relation from ∼21,000 galaxies in the SDSS. The squares in each plot are the median metallicity for data sorted into 30 mass bins. The dashed line in the left panel is a quadratic fit to the binned data. The dashed line in the right panel is a linear fit to the binned data. The dot-dashed line in the right panel is a linear fit to the data with $M_B > -20$.

differences resulting from the various metallicity diagnostics and calibrations have ostensibly been resolved by KE08. It should be noted however that it still remains uncertain whether relations calibrated using local galaxy samples are valid at higher redshifts. Care must be taken when comparing samples as selections effects lead to non-trivial differences in the determination of the MZ relation. We attempt to manage some of the differences arising from selection bias and different diagnostics by redetermining the local MZ relation from the SDSS data release 7 (Abazajian et al. 2009, http://www.mpa-garching.mpg.de/SDSS/DR7/) using similar selection cuts and the same metallicity calibration as our DEEP2 data set.

The SDSS DR7 consists of ∼818,000 galaxies spanning $0 < z < 0.7$. The emission-line EWs and galaxy stellar masses are calculated by the MPA/JHU group and are publicly available on the SDSS DR7 website. The EWs have been corrected for stellar absorption. The *ugriz* fiber and C model magnitudes (recommended for galaxy photometry) are also provided. We determine the stellar masses by fitting the photometry to population synthesis models using the Le Phare code (see Section 3.1).

We select galaxies by constraining the redshift such that $0.04 < z < 0.1$. The lower limit is imposed to minimize aperture effects. Furthermore, we follow the method of KE08 whereby we determine the *g*-band fiber covering fraction by comparing the fiber and model magnitudes. KE08 determine that a 20% covering fraction is insufficient to avoid aperture bias. We require a larger aperture fiber covering fraction of >30% in order to further reduce aperture effects. For the selected sample the median covering fraction is 38%. The upper redshift limit is imposed in order to minimize evolutionary effects and because the star-forming sample is found to be incomplete at higher redshifts (Kewley et al. 2006).

In order to minimize selection biases when comparing, we impose a similar selection criteria as applied to the DEEP2 sample. We require that SN Hβ > 3, $\sigma_{r23} < 2$, and EW(Hβ) > 4 Å. The SDSS data have much broader spectral coverage. For all galaxies in our redshift range we use the star-forming galaxies defined by the Kewley et al. (2006) classification scheme. KE08 showed that MZ relation derived from the SDSS data using the log([N II]/O[II]) ratio is insensitive to the classification scheme used to identify and remove AGN. The selected SDSS data sample consists of ∼21,000 galaxies. The median EW(Hβ) and S/N Hβ of our selected sample is 8.9 and 20.7, respectively.

Figure 13 shows the local MZ and LZ relations derived from the selected SDSS sample. The metallicities have been derived using the EWs as described in Section 3.3. We place galaxies on the lower R_{23} branch when log([N II]/O[II]) < −1.2 (KE08). An insignificant fraction (25/21816) are on the lower branch. The fits to the relations use the same bootstrapping method described in Section 4. For the MZ relation, the data are binned in 30 equally populated mass bins. From the left panel of Figure 13 it can be seen that the lowest mass bin suggests a turnover in the relation. This may be a result of incompleteness, though this is difficult to establish from these data. Whatever the case, the lowest mass bin is excluded when fitting the MZ relation. The MZ relation is given by

$$12 + \log(\mathrm{O/H}) = (9.051 \pm 0.001) + (0.151 \pm 0.004)\,\mathrm{x} - (0.104 \pm 0.006)\,\mathrm{x}^2, \quad \text{(A6)}$$

where $x = \log(M_*) - 10$, the logarithm of the stellar mass in solar mass units zero pointed to reduce the covariance of the parameters by subtracting 10. The dashed line in the left panel of Figure 13 shows this fit.

The LZ relation is determined by sorting the data into 30 equally populated luminosity bins. The relation is shown in the right panel of Figure 13. The dashed curve is a linear fit to the data and is parameterized by

$$12+\log(\mathrm{O/H}) = (9.089\pm0.003)-(0.0833\pm0.002)\mathrm{X_B}, \quad \text{(A7)}$$

where $X_B = M_B + 21$. The data turn over at $M_B \sim -20$, presumably due to the more fundamental turnover observed in the MZ relation at the higher masses. If we fit the LZ relation in the linear part of the relation, $M_B > -20$, the fit is

$$12 + \log(\mathrm{O/H}) = (9.131 \pm 0.006) - (0.105 \pm 0.003)\mathrm{X_B}. \quad \text{(A8)}$$

This dot-dashed line in the right panel of Figure 13 shows this fit.

REFERENCES

Abazajian, K. N., et al. 2009, ApJS, 182, 543
Ažusienis, A., & Straižys, V. 1969, SvA, 13, 316
Baldry, I. K., Glazebrook, K., Brinkmann, J., Ivezić, Ž., Lupton, R. H., Nichol, R. C., & Szalay, A. S. 2004, ApJ, 600, 681
Bell, E. F., McIntosh, D. H., Katz, N., & Weinberg, M. D. 2003, ApJS, 149, 289
Blanton, M. R. 2006, ApJ, 648, 268

Brooks, A. M., Governato, F., Booth, C. M., Willman, B., Gardner, J. P., Wadsley, J., Stinson, G., & Quinn, T. 2007, ApJ, 655, L17
Bruzual, G., & Charlot, S. 2003, MNRAS, 344, 1000
Bundy, K., et al. 2006, ApJ, 651, 120
Buser, R. 1978, A&A, 62, 411
Calzetti, D., Armus, L., Bohlin, R. C., Kinney, A. L., Koornneef, J., & Storchi-Bergmann, T. 2000, ApJ, 533, 682
Carollo, C. M., & Lilly, S. J. 2001, ApJ, 548, L153
Chabrier, G. 2003, PASP, 115, 763
Charlot, S., & Longhetti, M. 2001, MNRAS, 323, 887
Coil, A. L., Newman, J. A., Kaiser, N., Davis, M., Ma, C.-P., Kocevski, D. D., & Koo, D. C. 2004, ApJ, 617, 765
Conroy, C., Gunn, J. E., & White, M. 2009, ApJ, 699, 486
Cowie, L. L., & Barger, A. J. 2008, ApJ, 686, 72
Cowie, L. L., Songaila, A., Hu, E. M., & Cohen, J. G. 1996, AJ, 112, 839
Davis, M., et al. 2003, Proc. SPIE, 4834, 161
de Rossi, M. E., Tissera, P. B., & Scannapieco, C. 2007, MNRAS, 374, 323
Drory, N., Bender, R., & Hopp, U. 2004, ApJ, 616, L103
Erb, D. K., Shapley, A. E., Pettini, M., Steidel, C. C., Reddy, N. A., & Adelberger, K. L. 2006, ApJ, 644, 813
Faber, S. M., et al. 2003, Proc. SPIE, 4841, 1657
Faber, S. M., et al. 2007, ApJ, 665, 265
Ferland, G. J. 1996, Hazy, A Brief Introduction to Cloudy 90 (Lexington, KY: Univ Kentucky Internal Report)
Fontana, A., et al. 2004, A&A, 424, 23
Garnett, D. R. 2002, ApJ, 581, 1019
Garnett, D. R., Shields, G. A., Skillman, E. D., Sagan, S. P., & Dufour, R. J. 1997, ApJ, 489, 63
Hogg, D. W., et al. 2003, ApJ, 585, L5
Horne, K. 1986, PASP, 98, 609
Hoversten, E. A., & Glazebrook, K. 2008, ApJ, 675, 163
Ilbert, O., et al. 2005, A&A, 439, 863
Ilbert, O., et al. 2010, ApJ, 709, 644
Impey, C., & Bothun, G. 1997, ARA&A, 35, 267
Jansen, R. A., Fabricant, D., Franx, M., & Caldwell, N. 2000, ApJS, 126, 331
Kauffmann, G., & Charlot, S. 1998, MNRAS, 294, 705
Kennicutt, R. C., Jr. 1992, ApJS, 79, 255
Kewley, L. J., & Dopita, M. A. 2002, ApJS, 142, 35
Kewley, L. J., & Ellison, S. L. 2008, ApJ, 681, 1183
Kewley, L. J., Groves, B., Kauffmann, G., & Heckman, T. 2006, MNRAS, 372, 961
Kewley, L. J., Rupke, D., Jabran Zahid, H., Geller, M. J., & Barton, E. J. 2010, ApJ, 721, L48
Kobulnicky, H. A., Kennicutt, R. C., Jr., & Pizagno, J. L. 1999, ApJ, 514, 544
Kobulnicky, H. A., & Kewley, L. J. 2004, ApJ, 617, 240
Kobulnicky, H. A., & Koo, D. C. 2000, ApJ, 545, 712
Kobulnicky, H. A., & Phillips, A. C. 2003, ApJ, 599, 1031
Kobulnicky, H. A., et al. 2003, ApJ, 599, 1006
Köppen, J., Weidner, C., & Kroupa, P. 2007, MNRAS, 375, 673
Kroupa, P. 2001, MNRAS, 322, 231
Lamareille, F., Mouhcine, M., Contini, T., Lewis, I., & Maddox, S. 2004, MNRAS, 350, 396
Lamareille, F., et al. 2009, A&A, 495, 53
Larson, R. B. 1974, MNRAS, 169, 229
Larson, R. B., & Dinerstein, H. L. 1975, PASP, 87, 911
Lequeux, J., Peimbert, M., Rayo, J. F., Serrano, A., & Torres-Peimbert, S. 1979, A&A, 80, 155
Lilly, S. J., Le Fevre, O., Crampton, D., Hammer, F., & Tresse, L. 1995, ApJ, 455, 50
Maier, C., Meisenheimer, K., & Hippelein, H. 2004, A&A, 418, 475
Maiolino, R., et al. 2008, A&A, 488, 463
Mannucci, F., et al. 2009, MNRAS, 398, 1915
Markwardt, C. B. 2009, in ASP Conf. Ser. 411, Astronomical Data Analysis Software and Systems (ADASS) XVIII, ed. D. Bohlender, D. Durand, & P. Dowler (San Francisco, CA: ASP), 251
Melbourne, J., Phillips, A. C., Harker, J., Novak, G., Koo, D. C., & Faber, S. M. 2007, ApJ, 660, 81
Meurer, G. R., et al. 2009, ApJ, 695, 765
Mouchine, M., Gibson, B. K., Renda, A., & Kawata, D. 2008, arXiv:0801.2476
Noeske, K. G., et al. 2007a, ApJ, 660, L47
Noeske, K. G., et al. 2007b, ApJ, 660, L43
Oppenheimer, B. D., & Davé, R. 2008, MNRAS, 387, 577
Osterbrock, D. E. (ed.) 1989, in Astrophysics of Gaseous Nebulae and Active Galactic Nuclei (Sausalito, CA: Univ. Science Books), 422
Pagel, B. E. J. (ed.) 1997, in Nucleosynthesis and Chemical Evolution of Galaxies (Cambridge: Cambridge Univ. Press), 392
Pagel, B. E. J., Edmunds, M. G., Blackwell, D. E., Chun, M. S., & Smith, G. 1979, MNRAS, 189, 95
Pérez-Montero, E., et al. 2009, A&A, 495, 73
Pettini, M., Shapley, A. E., Steidel, C. C., Cuby, J.-G., Dickinson, M., Moorwood, A. F. M., Adelberger, K. L., & Giavalisco, M. 2001, ApJ, 554, 981
Salpeter, E. E. 1955, ApJ, 121, 161
Salzer, J. J., Lee, J. C., Melbourne, J., Hinz, J. L., Alonso-Herrero, A., & Jangren, A. 2005, ApJ, 624, 661
Savaglio, S., et al. 2005, ApJ, 635, 260
Schechter, P. 1976, ApJ, 203, 297
Schmidt, M. 1963, ApJ, 137, 758
Searle, L., & Sargent, W. L. W. 1972, ApJ, 173, 25
Shapley, A. E., Coil, A. L., Ma, C.-P., & Bundy, K. 2005, ApJ, 635, 1006
Shapley, A. E., Erb, D. K., Pettini, M., Steidel, C. C., & Adelberger, K. L. 2004, ApJ, 612, 108
Simard, L., et al. 2002, ApJS, 142, 1
Skillman, E. D., Kennicutt, R. C., & Hodge, P. W. 1989, ApJ, 347, 875
Somerville, R. S., & Primack, J. R. 1999, MNRAS, 310, 1087
Springel, V., & Hernquist, L. 2003, MNRAS, 339, 289
Strateva, I., et al. 2001, AJ, 122, 1861
Tremonti, C. A., et al. 2004, ApJ, 613, 898
van den Bergh, S. 1962, AJ, 67, 486
van Dokkum, P. G. 2008, ApJ, 674, 29
Weiner, B. J., et al. 2006, ApJ, 653, 1049
Weiner, B. J., et al. 2007, ApJ, 660, L39
Willmer, C. N. A., et al. 2006, ApJ, 647, 853
Zaritsky, D., Kennicutt, R. C., Jr., & Huchra, J. P. 1994, ApJ, 420, 87